Phase-augmented digital image correlation for high-accuracy deformation measurement: Theory, validation, and application to constitutive law learning

Rahul Danda [a], Xinxin Wu [b], Sheng Mao [b,*], Yin Zhang [b,*], Ting Zhu [a], Shuman Xia [a,*]

[a] *Woodruff School of Mechanical Engineering, Georgia Institute of Technology, Atlanta, GA 30332, USA*
[b] *Department of Mechanics and Engineering Science, College of Engineering, Peking University, 100871, Beijing, China*

ABSTRACT

Digital image correlation (DIC) is a prominent technique for full-field, non-contact deformation characterization. Despite its sub-pixel sensitivity for displacement measurement, conventional DIC often suffers from inadequate signal-to-noise ratios (SNRs) when measuring small deformations in stiff and/or brittle materials. This work presents phase-augmented DIC (PA-DIC), a novel method that integrates coherent illumination with image correlation to achieve measurement accuracy that surpasses that of conventional DIC. Unlike conventional DIC, which relies on non-coherent illumination to maintain gray-level conservation during deformation, PA-DIC leverages speckle phase information to measure displacement with improved sensitivity. We applied PA-DIC to characterize rigid-body rotation and non-uniform tensile deformation, validating its high accuracy and reliability. Furthermore, we demonstrated its application for machine learning of an orthotropic elastic constitutive relationship. This was achieved using a hybrid finite element method and neural network (FEM-NN) optimization framework supplied with high-accuracy non-uniform strain data from PA-DIC. With its exceptional measurement accuracy, PA-DIC opens new possibilities for advanced full-field measurement and data-driven material characterization in the small deformation regime.

1. Introduction

Full-field, non-contact measurement is increasingly used for the deformation characterization of advanced materials and structures (Avril et al., 2008; Grediac, 2004; Hung and Ho, 2005; Johnson et al., 1998; McClung et al., 2011; Nave and Barnett, 2004; Rastogi, 2000). The digital image correlation (DIC) technique stands out as a powerful tool for such measurement (Chu et al., 1985; Pan et al., 2009; Peters and Ranson, 1982b; Sutton et al., 1986). Combined with various imaging methods, DIC has been utilized across a wide spectrum of applications and length scales, including landslide monitoring using high-resolution satellite imagery (Delacourt et al., 2004), microscale characterization of biological tissues (Krehbiel et al., 2010), and nanoscale deformation analysis of semiconductor materials and polycrystalline metals (Chasiotis and Knauss, 2002; Kammers and Daly, 2013; Wang et al., 2015).

In a two-dimensional (2D) DIC analysis, the displacement distribution of a test specimen is obtained by correlating two digital gray-scale speckle images taken before and after deformation (Chu et al., 1985; Peters and Ranson, 1982a; Sutton et al., 1983). Depending

---

on how deformation kinematics are treated, existing DIC algorithms can be classified into two major groups: local DIC and global DIC. In local DIC, a region of interest (ROI) in the undeformed (reference) image is segmented into an array of subsets, which are typically square-shaped and uniformly spaced. The displacement of each subset is determined by searching for a subset in the deformed configuration that has the highest correlation with the original subset. The affine mapping from the original to deformed subset is usually assumed, so that higher-order gradient terms are neglected. Global DIC, on the other hand, is based on a global description of the deformation kinematics over the entire ROI (Besnard et al., 2006; Sun et al., 2005). It approximates the displacement field under measurement by a trial displacement field with a finite number of degrees of freedom (DOFs). This treatment transforms the DIC problem into nonlinear, multi-variable minimization with respect to the DOF values.

Most commercial and open-source DIC programs to date have adopted subset-based local DIC due to its high computational efficiency, ease of implementation, and longer historical development compared to global DIC methods. Nevertheless, global DIC offers several distinct advantages, making it particularly well-suited for complex deformation analyses. Firstly, the global treatment of kinematics employed in global DIC automatically enforces deformation compatibility, resulting in smoother strain fields compared to those obtained with local DIC methods. Additionally, local DIC has been shown to be less effective for analyzing highly heterogeneous deformation, as the affine kinematics assumed by local DIC cannot adequately capture sharp changes in deformation gradient within a subset (Hild and Roux, 2012; Pan et al., 2015). Such cases are better handled using global DIC, which can capture more complex deformation modes with spatially varying or adaptive meshes (Yang and Bhattacharya, 2019b). Furthermore, the same discretization scheme can be used for both global DIC experiments and numerical modeling, allowing for direct comparison and minimizing discretization errors. In light of these considerations, a hybrid local/global DIC approach has recently been developed to combine the efficiency of local DIC with the kinematic compatibility of global DIC, employing an augmented Lagrangian framework (Yang and Bhattacharya, 2019a).

Using image correlation rather than tracking the movement of individual pixels allows full-field displacement data to be obtained at the sub-pixel level. However, when analyzing small deformations in stiff and/or brittle materials, conventional DIC (C-DIC) methods often produce noisy and unreliable displacement and strain data due to very limited displacement ranges. In this study, we present a novel DIC method that leverages phase information from coherent illumination to achieve unprecedented accuracy in displacement measurement and also demonstrate its application in machine learning for constitutive laws. In a C-DIC analysis, non-coherent illumination is typically required to maintain the assumption of gray-level conservation during deformation (Fig. 1(a)). When a rough surface is illuminated with coherent structured light, a speckle image forms due to light scattering and interference on the surface. Introducing a deformation mapping to the surface causes image speckles to change their phases and, consequently, their intensities (Fig. 1(b)). In other words, the changes in image intensity encode full-field displacement information with the high sensitivity of optical interferometry. We developed a global image correlation-based method to decode this deformation information. We refer to this new method as phase-augmented DIC (PA-DIC) and present here its theory, error assessments, and application in data-driven learning of an orthotropic elastic constitutive law.
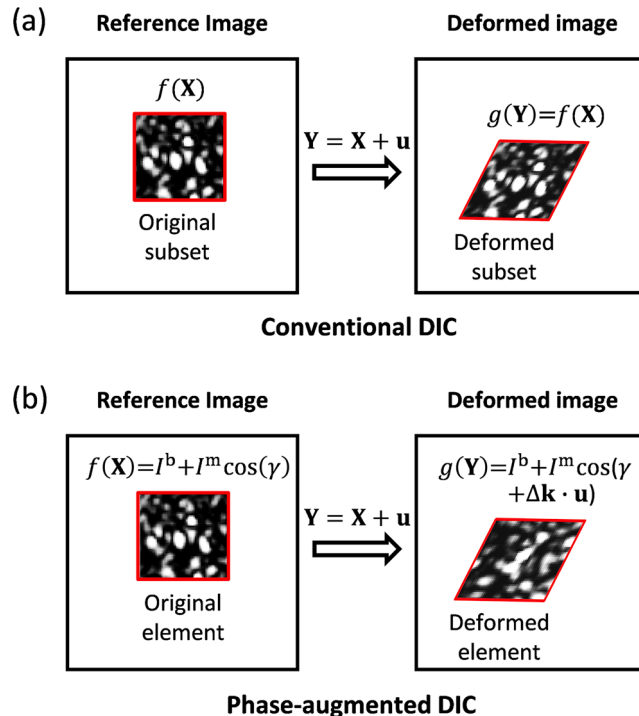

Fig. 1. Comparison between (a) conventional digital image correlation (C-DIC) and (b) phase-augmented DIC (PA-DIC).
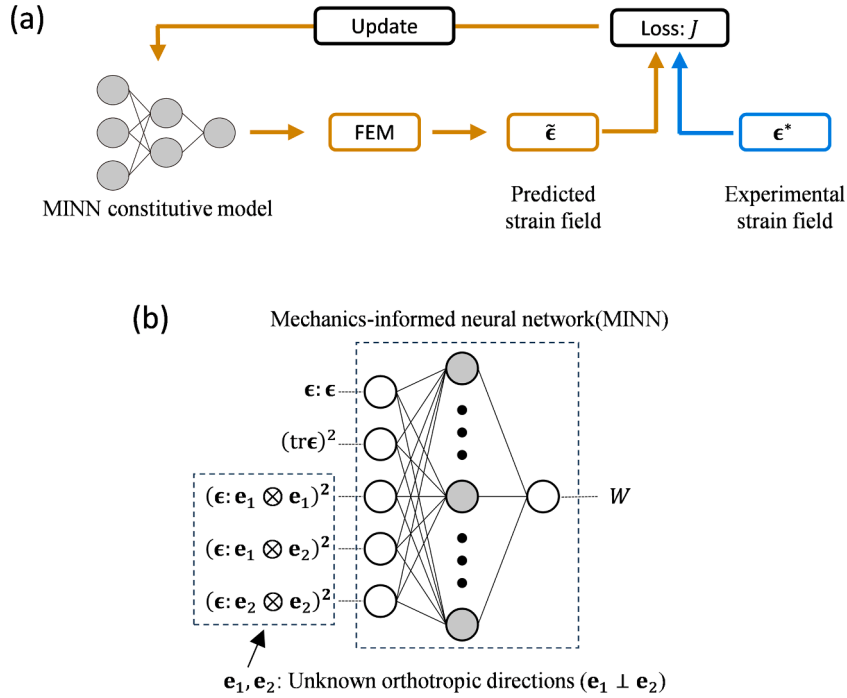
Fig. 2. (a) A hybrid FEM-NN optimization framework used to train (b) a MINN constitutive model, using ground truth strain data ϵ^* obtained from PA-DIC.

In recent years, full-field deformation data from non-uniformly deformed specimens, covering a range of diverse stress-strain paths, have opened new avenues for the inverse extraction of constitutive information (Flaschel et al., 2022; Tung and Li, 2024). For example, using the Virtual Fields Method, Boddapati et al. identified the six stiffness parameters of 2D anisotropic materials from full-field displacement and global force data acquired in a single test (Boddapati et al., 2023). In addition, recent advancements in computational mechanics and machine learning have led to neural network (NN)-based approaches for learning constitutive relations from full-field data (Thakolkaran et al., 2022; Zhang et al., 2022). When developing such approaches, it is crucial to ensure the physical soundness of NN-based constitutive models; they should strictly enforce important physical constraints, such as material symmetry and objectivity by construction, which can be achieved through invariant-based constitutive modeling (Klein et al., 2022; Tac et al., 2022). To ensure that the partial differential equations corresponding to NN-based models are mathematically well-posed, Linden et al. proposed a physics-augmented neural network (PANN) architecture for hyperelastic materials (Linden et al., 2023; Thakolkaran et al., 2022), where polyconvexity of the energy storage function is ensured by using the input-convex neural network (ICNN) (Amos et al., 2017). Other conditions, such as volumetric growth and stress-free conditions, are also ensured either through additional analytic functions or by constraining the network's weights.

In this work, we applied PA-DIC to acquire high-fidelity infinitesimal strain ($\sim 10^{-4}$) data of an orthotropic material under elastic indentation loading and input these data into a physically sensible mechanics-informed neural network (MINN) (Wu et al., 2024) to identify the material's constitutive relationship. By constructing appropriate invariants from the infinitesimal strain tensor as inputs, the MINN constitutive model inherently satisfies the physical constraints of convexity, material symmetry, and stress-free conditions. A hybrid finite element method (FEM)-NN optimization framework was used to train the MINN model, and the material parameters obtained were compared with those measured through conventional uniaxial loading.

The remainder of the paper is organized as follows. In Section 2, we describe the working principle of PA-DIC and introduce the hybrid FEM-NN optimization framework for physics-constrained constitutive law learning. Section 3 details the experimental implementation of PA-DIC, including the optical setup employed, as well as information on specimen fabrication and mechanical testing protocols. Section 4 presents validation and performance results, focusing on the error assessments of PA-DIC and the outcomes of constitutive law learning using high-accuracy PA-DIC measurement and FEM-NN. We provide discussion in Section 5 and draw conclusions in Section 6.

2. Theory

2.1. Phase-augmented digital image correlation

Under illumination by two interfering coherent beams, the intensity distribution of a speckle image before deformation is given by

$$f(\mathbf{X}) = I^{\mathrm{b}}(\mathbf{X}) + I^{\mathrm{m}}(\mathbf{X})\cos(\gamma(\mathbf{X})), \tag{1}$$

in which γ is the speckle phase, and I^{b} and I^{m} are the background and modulation intensities, respectively. Imposing a deformation mapping $\mathbf{X} \rightarrow \mathbf{Y}$ (Fig. 1(b)), the intensity of the deformed image becomes

$$g(\mathbf{Y}) = I^{\mathrm{b}}(\mathbf{X}) + I^{\mathrm{m}}(\mathbf{X})\cos(\gamma(\mathbf{X}) + \Delta\mathbf{k} \cdot \mathbf{u}(\mathbf{X})), \tag{2}$$

where $\mathbf{u} = \mathbf{Y} - \mathbf{X}$ is the displacement field and $\Delta\mathbf{k}$ is the difference between the angular wave-vectors of the two illumination beams. Traditionally, an approach known as electronic speckle pattern interferometry (ESPI) has been used to process these speckle images through multi-step phase shifting (Cloud, 1998). Under the small-deformation assumption $\mathbf{X} \approx \mathbf{Y}$, ESPI extracts the deformation-induced phase change on a pixel-by-pixel basis, from which the displacement in the direction of $\Delta\mathbf{k}$ can be obtained. Despite its high sensitivity, ESPI has severe disadvantages related to the nature of speckles, including speckle noise and the ease of speckle decorrelation. In this work, we achieve full-field, high-accuracy 2D deformation measurement through image correlation, which is based on minimizing the following sum-of-squared-differences (SSD) cost function, E^2, over the ROI (denoted as R):

$$E^2 = \sum_i \int_R E_i^2 d\mathbf{X}$$

$$= \sum_i \int_R \left[I_i^{\mathrm{b}}(\mathbf{X}) + I_i^{\mathrm{m}}(\mathbf{X})\cos(\gamma_i(\mathbf{X}) + \Delta\mathbf{k}_i \cdot \mathbf{u}(\mathbf{X})) - g_i(\mathbf{X} + \mathbf{u}(\mathbf{X})) \right]^2 d\mathbf{X}. \tag{3}$$

Here, the subscript ($i = 1$ or 2) indicates an orthogonal in-plane direction, E_i represents the residual in the i-th direction, and $\Delta\mathbf{k}_i$ is the wave-vector difference in the i-th direction, which determines the displacement measurement sensitivity along that direction.

Nonlinear minimization of Eq. (3) with respect to $\mathbf{u}$ poses a challenge due to the multiple local minima introduced by the periodicity of the cosine term. We resolve this issue by devising an iterative phase retrieval scheme. Denoting $\mathbf{u}^{(n)}$ as the displacement at the n-th iteration and $\delta\mathbf{u}$ as the increment for the next iteration, we expand the cosine term and approximate g_i to the first order to obtain

$$E_i \approx I_i^{\mathrm{b}} + I_i^{\mathrm{m}}\cos(\gamma_i + \Delta\mathbf{k}_i \cdot \mathbf{u}^{(n)})\cos(\Delta\mathbf{k}_i \cdot \delta\mathbf{u}) - I_i^{\mathrm{m}}\sin(\gamma_i + \Delta\mathbf{k}_i \cdot \mathbf{u}^{(n)})\sin(\Delta\mathbf{k}_i \cdot \delta\mathbf{u})$$

$$- g_i(\mathbf{X} + \mathbf{u}^{(n)}) - \nabla g_i \cdot \delta\mathbf{u}, \tag{4}$$

in which ∇ denotes the gradient operator. We treat $p_i = \cos(\Delta\mathbf{k}_i \cdot \delta\mathbf{u})$ and $q_i = \sin(\Delta\mathbf{k}_i \cdot \delta\mathbf{u})$ as independent minimization variables, in addition to $\delta\mathbf{u}$. The variable vector is defined as

$$\mathbf{a} = \begin{bmatrix} p_1 & q_1 & p_2 & q_2 & \delta u_1 & \delta u_2 \end{bmatrix}^{\mathrm{T}}, \tag{5}$$

which is spatially discretized via a finite element (FE) formulation as $\mathbf{a}(\mathbf{X}) = \mathbf{N}(\mathbf{X})\mathbf{A}$. Here, $\mathbf{N}(\mathbf{X})$ is the global shape function matrix associated with a finite element mesh, and $\mathbf{A}$ is the nodal variable vector. Minimization of the cost function with respect to $\mathbf{A}$ results in a set of linear equations:

$$\left(\int_R \mathbf{N}^{\mathrm{T}}\mathbf{B}\mathbf{B}^{\mathrm{T}}\mathbf{N}d\mathbf{X} \right)\mathbf{A} = \int_R \mathbf{N}^{\mathrm{T}}\mathbf{B}\begin{bmatrix} g_1 - I_1^{\mathrm{b}} \\ g_2 - I_2^{\mathrm{b}} \end{bmatrix}d\mathbf{X}, \tag{6}$$

in which

$$\mathbf{B} = \frac{\partial\begin{bmatrix} E_1 & E_2 \end{bmatrix}}{\partial\mathbf{a}}$$

$$= \begin{bmatrix} I_1^{\mathrm{m}}\cos(\gamma_1 + \Delta\mathbf{k}_1 \cdot \mathbf{u}^{(n)}) & -I_1^{\mathrm{m}}\sin(\gamma_1 + \Delta\mathbf{k}_1 \cdot \mathbf{u}^{(n)}) & 0 & 0 & -\frac{\partial g_1}{\partial x_1} & -\frac{\partial g_1}{\partial x_2} \\ 0 & 0 & I_2^{\mathrm{m}}\cos(\gamma_2 + \Delta\mathbf{k}_2 \cdot \mathbf{u}^{(n)}) & -I_2^{\mathrm{m}}\sin(\gamma_2 + \Delta\mathbf{k}_2 \cdot \mathbf{u}^{(n)}) & -\frac{\partial g_2}{\partial x_1} & -\frac{\partial g_2}{\partial x_2} \end{bmatrix}^{\mathrm{T}}. \tag{7}$$

Solving the linear system given by Eq. (6) yields the nodal variables, which are then interpolated using the shape functions to obtain the full-field solution.

The incremental displacement δu_i is encoded in p_i and q_i, and can be retrieved from them with high sensitivity according to

$$\delta u_i = \frac{1}{|\Delta \mathbf{k}_i|} \operatorname{atan2}\left(q_i, p_i\right),$$

(8)

where atan2 is the quadrant-corrected arctan function. δu_i obtained from Eq. (8) is wrapped to the interval $\left(-\frac{\pi}{|\Delta \mathbf{k}_i|}, \frac{\pi}{|\Delta \mathbf{k}_i|}\right]$ due to the range limitation of the atan2 function. The wrapped δu_i map is processed with an unwrapping algorithm based on the fast cosine transformation (FCT) (Ghiglia and Romero, 1994) to yield the unwrapped incremental displacement, which is then added to the current estimate to yield the updated solution, i.e., $\mathbf{u}^{(n+1)} = \mathbf{u}^{(n)} + \delta \mathbf{u}$. This iterative procedure continues until the normalized Euclidean norm of $\delta \mathbf{u}$ falls below a pre-define threshold e^{tol}. For all deformation analyses reported in this work, we set $\mathbf{u}^{(0)} = 0$ as the initial guess and $e^{\text{tol}} = 10^{-5}$ pixel.

We note that the above phase retrieval scheme works most effectively when the speckle size, s, is sufficient large compared to a characteristic length determined by the wave vector difference, $l = 2\pi/|\Delta \mathbf{k}_i|$. For $l/s \ll 1$, the change in speckle intensity is much more sensitive to the phase change than to the speckle movement. Therefore, although $[p_i \quad q_i]$ and δu_i are theoretically dependent, they effectively behave as pseudo-independent variables during the minimization of the cost function (Eq. (3)). Moreover, the constraint $p_i^2 + q_i^2 = 1$ is effectively fulfilled through the cost function minimization, as a result of the large speckle size requirement. We verified the performance of our method through displacement measurements of a one-dimensional (1D) model specimen. Details of the verification and results are provided in the Appendix.

2.2. Neural network-based learning of constitutive relationships

We employ a hybrid FEM-NN optimization framework (Fig. 2(a)) for constitutive model identification from PA-DIC measurement. First, a NN-based strain energy density function W, which takes the invariants of the infinitesimal strain tensor as inputs (Fig. 2(b)), is initialized with random parameters $\mathbf{\Theta}$ including weights and biases, i.e., $W = W(\boldsymbol{\epsilon}, \mathbf{\Theta})$, where $\boldsymbol{\epsilon} = \frac{1}{2}[\nabla \mathbf{u} + (\nabla \mathbf{u})^{\mathrm{T}}]$ is the infinitesimal strain tensor. For orthotropic materials, W should be a function of the invariants $\boldsymbol{\epsilon} : \boldsymbol{\epsilon}$, $\operatorname{tr}\boldsymbol{\epsilon}$, $\boldsymbol{\epsilon} : \mathbf{e}_1 \otimes \mathbf{e}_1$, $\boldsymbol{\epsilon} : \mathbf{e}_1 \otimes \mathbf{e}_2$, and $\boldsymbol{\epsilon} : \mathbf{e}_2 \otimes \mathbf{e}_2$.
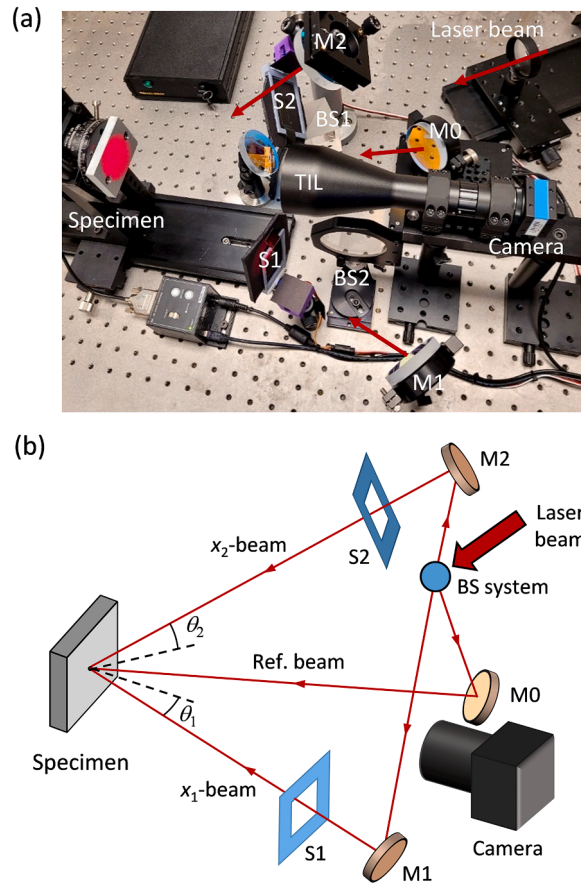

Fig. 3. (a) PA-DIC experimental setup for 2D high-accuracy deformation measurement. (b) Schematic of the optical arrangement illustrating beam paths. BS: beamsplitter, M: mirror, S: shutter, TIL: telecentric imaging lens.

Here, $\mathbf{e}_1 = [\cos(\varphi),\ \sin(\varphi)]$ and $\mathbf{e}_2 = [-\sin(\varphi),\ \cos(\varphi)]$ are the orthotropic directions, and φ is the orthotropic angle, which also needs to be identified through the hybrid FEM-NN framework, i.e., $\varphi \in \boldsymbol{\Theta}$. With this parametrized strain energy density W, the displacement field of the material under external loading can be obtained by solving the weak form of the equilibrium equation using the FEM on a discretized mesh over the material domain Ω (Hughes, 2003), i.e., find $\mathbf{u} \in \mathscr{U}$ such that for $\forall \mathbf{v} \in \mathscr{V}$,

$$\int \boldsymbol{\sigma}(\boldsymbol{\epsilon},\ \boldsymbol{\Theta}) : \nabla \mathbf{v} d\mathbf{X} - \int_{\partial\Omega^{\mathbf{t}}} \mathbf{t} \cdot \mathbf{v} d\mathbf{S} = 0, \tag{9}$$

where $\boldsymbol{\sigma} = \partial W/\partial\boldsymbol{\epsilon}$ is the Cauchy stress tensor and $\mathbf{t}$ denotes the traction applied on the boundary $\partial\Omega^{\mathbf{t}}$, and

$$\mathscr{U} = \left\{ \mathbf{u} \in H^1(\Omega) \big| \mathbf{u} = \mathbf{u}_{\mathrm{b}} \text{ on } \partial\Omega^{\mathbf{u}} \right\}, \tag{10a}$$

$$\mathscr{V} = \left\{ \mathbf{v} \in H^1(\Omega) \big| \mathbf{v} = 0 \text{ on } \partial\Omega^{\mathbf{u}} \right\}. \tag{10b}$$

Here, $\partial\Omega^{\mathbf{u}}$ denotes the boundary where the displacement condition is prescribed.

We evaluate a loss function J, which quantifies the error between the ground truth displacement field $\mathbf{u}^*$, measured by PA-DIC, and the predicted displacement $\widetilde{\mathbf{u}}$ obtained from solving Eq. (9) with the strain energy density $W(\boldsymbol{\epsilon},\ \boldsymbol{\Theta})$ under training. To eliminate the influence of rigid-body motions in experimental measurement, we use the corresponding strains to define J as follows

$$J = \sum_j \frac{\int_R \left(\widetilde{\boldsymbol{\epsilon}}_j - \boldsymbol{\epsilon}_j^* \right) : \left(\widetilde{\boldsymbol{\epsilon}}_j - \boldsymbol{\epsilon}_j^* \right) d\mathbf{X}}{\int_R \boldsymbol{\epsilon}_{\mathrm{m}}^* : \boldsymbol{\epsilon}_{\mathrm{m}}^* d\mathbf{X}}. \tag{11}$$

Here, j denotes the loading step, $R \in \Omega$ is the ROI over which the displacement field is measured, and $\boldsymbol{\epsilon}_{\mathrm{m}}^*$ is the maximum strain used to normalize J. Note that the small-deformation assumption inherent in this approach does not accommodate objectivity under large rigid-body rotations.

Next, the gradient of J with respect to $\boldsymbol{\Theta}$ is computed using the adjoint method (Mitusch et al., 2019). $\boldsymbol{\Theta}$ is updated by the L-BFGS-B optimization method (Byrd et al., 1995) to minimize the loss function using its gradient $\mathrm{d}J/\mathrm{d}\boldsymbol{\Theta}$. This operation is repeated iteratively until the L-BFGS-B algorithm converges or the number of iterations exceeds a threshold. A revised MINN (Wu et al., 2024) for small strains is employed as our NN model to ensure the physical sensibility of the constitutive model. Fig. 2(b) shows the architecture of the MINN used, which consists of one input layer with five neurons, one output layer with one neuron, and one hidden layer with a varied number of neurons to investigate the effects of model size. The MINN model is based on the ICNN (Amos et al., 2017), where the output of the network is a convex and non-decreasing function of its inputs. This convexity is achieved by using non-negative weights and convex, non-decreasing activation function in the NN. Here, we employ the Softplus function as the activation function

$$f(x) = \ln(1 + e^x). \tag{12}$$

For 2D orthotropic elasticity considered in this work, we select the following five invariants as the inputs of the MINN

$$\mathscr{I}_{\mathrm{ortho}} = \left\{ \boldsymbol{\epsilon} : \boldsymbol{\epsilon},\ (\mathrm{tr}\boldsymbol{\epsilon})^2,\ (\boldsymbol{\epsilon} : \mathbf{e}_1 \otimes \mathbf{e}_1)^2,\ (\boldsymbol{\epsilon} : \mathbf{e}_1 \otimes \mathbf{e}_2)^2,\ (\boldsymbol{\epsilon} : \mathbf{e}_2 \otimes \mathbf{e}_2)^2 \right\}, \tag{13}$$

which are all convex with respect to $\boldsymbol{\epsilon}$. As a result, the strain energy density W derived from the MINN is also a convex function of $\boldsymbol{\epsilon}$. Additionally, this selection ensures that our model satisfies the zero-prestress condition, i.e., $\frac{\partial W}{\partial\boldsymbol{\epsilon}}\big|_{\boldsymbol{\epsilon}=0} = 0$.

The hybrid FEM-NN optimization framework was implemented with the open-source FEM library *FEniCS* (Alnæs et al., 2015), using first-order triangular elements under plane-stress conditions. Backpropagation for training the MINN was enabled by *dolfin-adjoint* (Mitusch et al., 2019), an operator-overloading algorithmic differentiation framework. The convergence tolerance for the loss function was set to 10^{-10}, and the maximum number of iterations was set to 100.

3. Experimentation

3.1. Experimental setup

Fig. 3 shows a 2D measurement setup built to implement the PA-DIC method. An input helium-neon laser beam of 15 mW (1144P-3581, JDSU, Milpitas, CA) is focused through a pinhole acting as a spatial filter and then collimated with a convex lens. The collimated

Table 1
3D printing settings for the orthotropic elastic indentation specimen

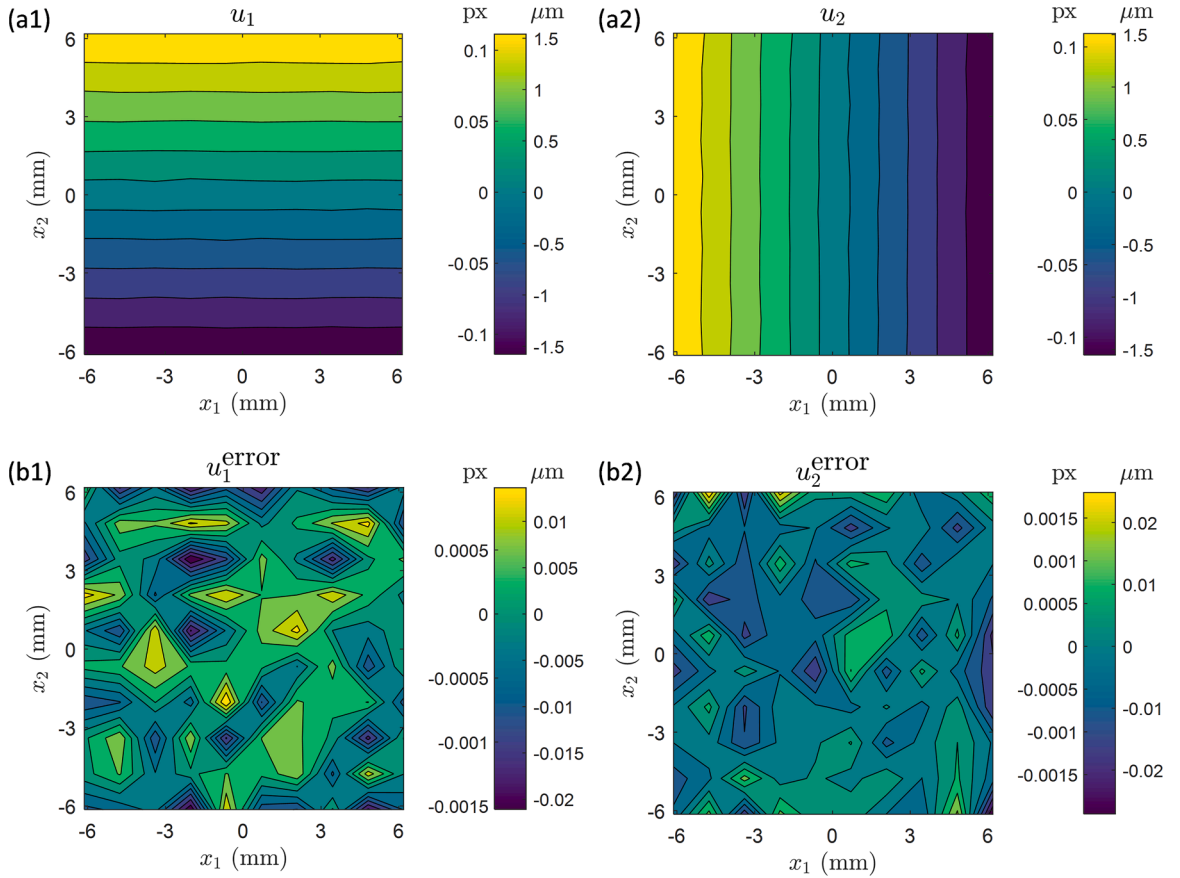| Material	Carbon fiber-reinforced PLA
Infill	100 %
Infill pattern	Rectilinear
Printing temperature	230 °C
Nozzle diameter	0.4 mm
Layer thickness	0.2 mm

Fig. 4. Displacement fields resulting from a small in-plane rigid-body rotation, measured by PA-DIC: (a1) horizontal displacement (u_1); (a2) vertical displacement (u_2); (b1) horizontal displacement error (u_1^{error}); (b2) vertical displacement error (u_2^{error}).

beam is split and redirected by a series of partially and fully reflecting mirrors, resulting in one reference beam and two beams for horizontal (x_1) and vertical (x_2) displacement measurement. The reference beam continuously illuminates a test specimen, while two mechanical shutters selectively activate either the x_1- or x_2-measurement beam at a time. Image acquisition is performed using a digital CMOS camera (DFK 72AUC02, Imaging Source, Charlotte, NC) equipped with a bi-telecentric lens (#56–675, Edmund Optics, Barrington, NJ) at a pixel scale of 13.82 μm/pixel. To minimize the effects of out-of-plane motion on speckle phase, each measurement beam and the reference beam illuminate the specimen surface at symmetric angles, with the camera bisecting the angle between them. Prior to specimen movement, the reference beam undergoes phase shifting of 0, $\pi/2$, π, and $3\pi/2$ with a piezoelectric nano-positioning stage (NPXY150Z10A, nPoint, Middleton, WI). The four-step phase-shifting method (Cloud, 1998) is employed to derive the background and modulation intensities along with the initial speckle phase necessary for image correlation, from the phase-shifted speckle images. The sensitivities of this PA-DIC setup are $|\Delta \mathbf{k}_1| = 6.92 \ \mu\text{m}^{-1}$ and $|\Delta \mathbf{k}_2| = 6.60 \ \mu\text{m}^{-1}$ for measuring horizontal and vertical displacements, respectively.

3.2. Specimen fabrication and mechanical testing

We performed rigid-body rotation (RBR) and tapered tension (TT) testing to evaluate the accuracy of the PA-DIC method, as well as indentation testing on a 3D-printed anisotropic polymeric specimen to demonstrate its application. The RBR specimen was a flat aluminum plate, with its surface polished using 300 grit sandpaper to create an appropriate surface texture for laser speckle generation. Shown in Fig. 8(a), the TT specimen features a tapering angle of 30° and was water jet cut from a 3.1 mm thick polymethyl methacrylate (PMMA) sheet. The indentation specimen, illustrated in Fig. 10(a), was 3D printed from polylactic acid (PLA) filament reinforced with short carbon fibers using the fused filament fabrication (FFF) process. The printing conditions are detailed in Table 1. The carbon fibers in the printed PLA specimen were highly aligned along the material deposition direction. The alignment of these fibers, combined with the layer-by-layer printing microstructure, resulted in strong anisotropic mechanical properties of the specimen (Ferreira et al., 2017). To facilitate PA-DIC measurement, one side of both the TT and indentation specimens was spray-painted with reflective metallic silver paint, which effectively scattered laser light to produce high-contrast speckle patterns. The laser intensity and camera exposure were adjusted to prevent oversaturation of the camera detector. In addition, the aperture size was adjusted to obtain a
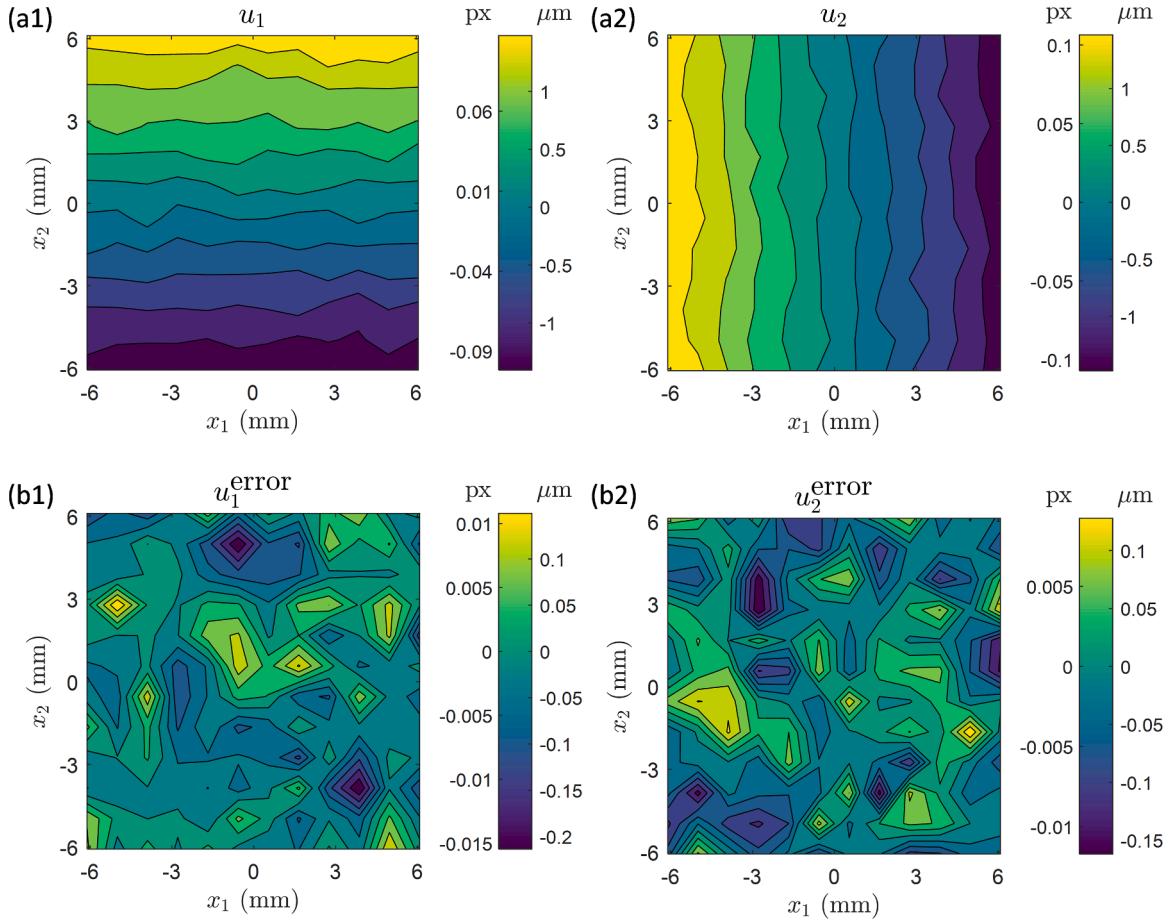
Fig. 5. Displacement fields resulting from a small in-plane rigid-body rotation, measured by conventional local DIC (CL-DIC): (a1) horizontal displacement (u_1); (a2) vertical displacement (u_2); (b1) horizontal displacement error (u_1^{error}); (b2) vertical displacement error (u_2^{error}).

speckle size of $s \approx 110$ μm, resulting in $l/s \approx 0.008$, which is well within the required range for large speckle sizes for PA-DIC (see the Appendix).

The RBR specimen underwent in-plane rotation using a high-precision rotation stage (481-A, Newport Corp., Irvine, CA), and the resulting rigid-body motion was measured by PA-DIC. The TT specimen was subjected to ramping tensile loading using a motorized test stand (ESM301 L, Mark-10 Corp., Copiague, NY), with the load incremented in 10 equal steps up to the maximum load. At each loading step, laser speckle images were acquired and correlated with the reference images for deformation measurement, using the displacement field from the previous loading step as the initial guess. The indentation specimen was tested by compressing it with a cylindrical steel indenter of 6.35 mm radius, following a similar load ramping and deformation analysis procedure as used for the TT specimen. The entire mechanical loading and optical measurement setup was placed on a floating optical table and inside an acoustic isolation enclosure to minimize external vibrations and noise.

4. Results

4.1. Error assessments

To assess the baseline measurement errors of PA-DIC, a small rigid-body rotation of 0.27 mrad was applied to the RBR specimen, creating linearly varying horizontal (u_1) and vertical (u_2) displacement fields. The laser speckle patterns used for PA-DIC are generated by light scattering and interference from rough surfaces, making them less prone to issues common with conventional DIC patterns, such as clumping or inhomogeneities. The primary factor controlling laser speckle patterns is the speckle size, which can be adjusted by varying the aperture size of the imaging lens. We conducted displacement analyses of the RBR specimen to assess measurement errors associated with two different speckle sizes: 7.9 and 9.7 pixels. Fig. 4(a1-a2) shows the contour plots of both displacement components measured with the speckle size of 7.9 pixels, using a grid mesh of square elements and a mesh size of 99 pixels (1.37 mm). Each contour plot is fairly smooth and exhibits a nearly constant gradient consistent with the applied rotation angle. The measurement errors in u_1 and u_2, depicted in Fig. 4(b1-b2), were obtained by subtracting the theoretical linear distributions from the measured displacements.
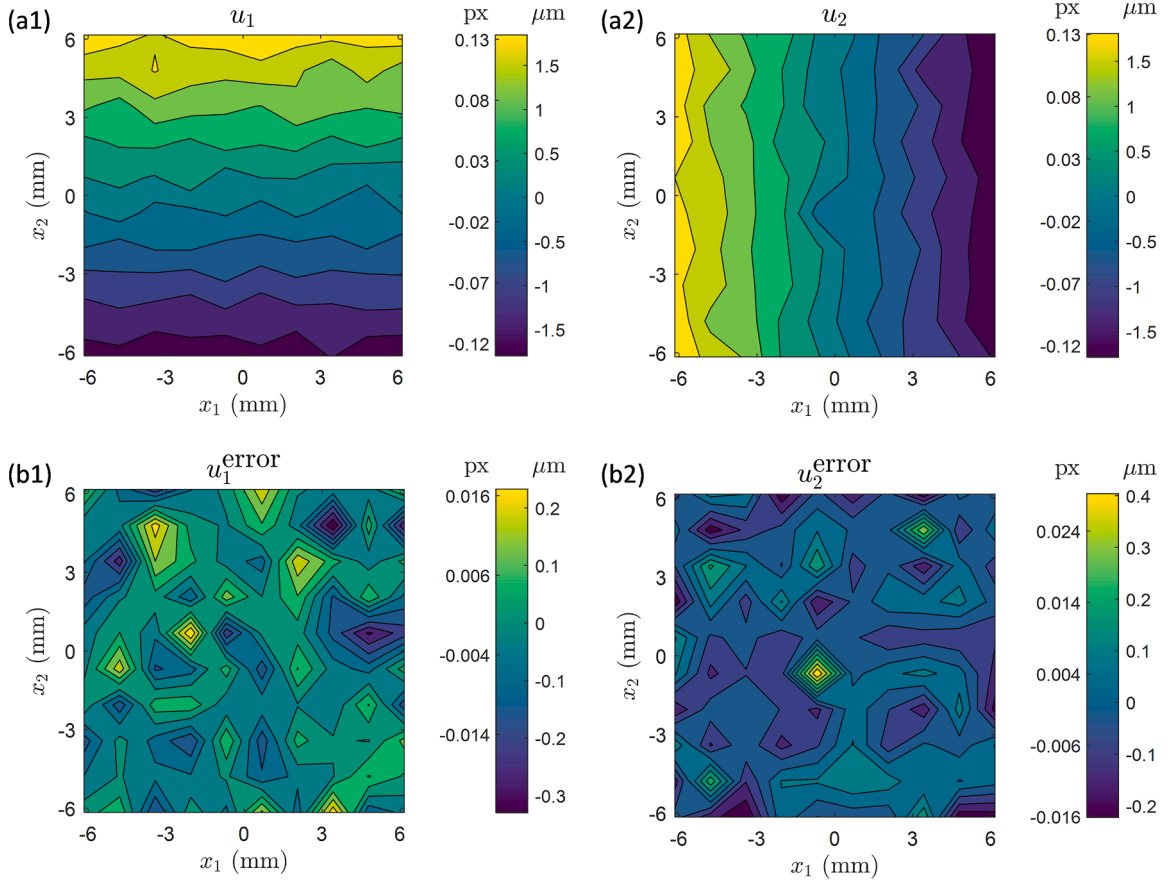
Fig. 6. Displacement fields resulting from a small in-plane rigid-body rotation, measured by conventional global DIC (CG-DIC): (a1) horizontal displacement (u_1); (a2) vertical displacement (u_2); (b1) horizontal displacement error (u_1^{error}); (b2) vertical displacement error (u_2^{error}).

Table 2
Comparison of displacement RMS errors for rigid-body rotation and stationary tests with different DIC methods

Test	DIC method	Speckle size (pixel)	Error in u_1 (pixel)	Error in u_2 (pixel)
Rigid-body rotation	PA-DIC	7.9	8.9×10^{-4}	9.9×10^{-4}
	CL-DIC	8.4	4.8×10^{-3}	4.9×10^{-3}
	CG-DIC	8.4	1.1×10^{-2}	1.1×10^{-2}
Stationary test	PA-DIC	7.9	2.9×10^{-4}	5.0×10^{-4}
	CL-DIC	8.4	4.8×10^{-3}	4.8×10^{-3}
	CG-DIC	8.4	1.0×10^{-2}	9.4×10^{-3}

The root-mean-square (RMS) values for the two error maps are 8.9×10^{-4} and 9.9×10^{-4} pixel, respectively. Increasing the speckle size to 9.7 pixels raises the RMS errors to 1.2×10^{-3} and 1.4×10^{-3}, respectively.

The performance of PA-DIC was evaluated against conventional global DIC (CG-DIC) and subset-based conventional local DIC (CL-DIC), which were employed to measure the same rigid-body movement. CL-DIC measurements were conducted using the commercial VIC-2D software (Correlated Solutions Inc.), while CG-DIC measurements employed an open-source DIC program (Yang and Bhat-tacharya, 2019a). A high-contrast speckle pattern required for the CG-DIC and CL-DIC analyses was created by first spray-painting the specimen surface white as a background, and then applying a black speckle pattern. To ensure a fair comparison between the three DIC methods, a subset size of 99 pixels was used for the CL-DIC measurement, matching the mesh size used for the CG-DIC and PA-DIC measurements. Additionally, the average speckle sizes were approximately the same: 8.4 pixels for CG-DIC and CL-DIC, and 7.9 pixels for PA-DIC. The results from the CL-DIC and CG-DIC measurements are summarized in Figs. 5 and 6. The displacement contours in Fig. 5(a1-a2) and Fig. 6(a1-a2) are much more irregular than those in Fig. 4(a1-a2). The RMS values of the error maps in Fig. 5 (b1-b2) and Fig. 6(b1-b2) range from 4.8×10^{-3} to 1.1×10^{-2} pixel, significantly higher than those obtained with PA-DIC.

To investigate the origin of the displacement errors in Figs. 4–6, we acquired consecutive speckle images of the RBR specimen while keeping it stationary and measured the associated errors using three different DIC methods. A comparison of the displacement RMS
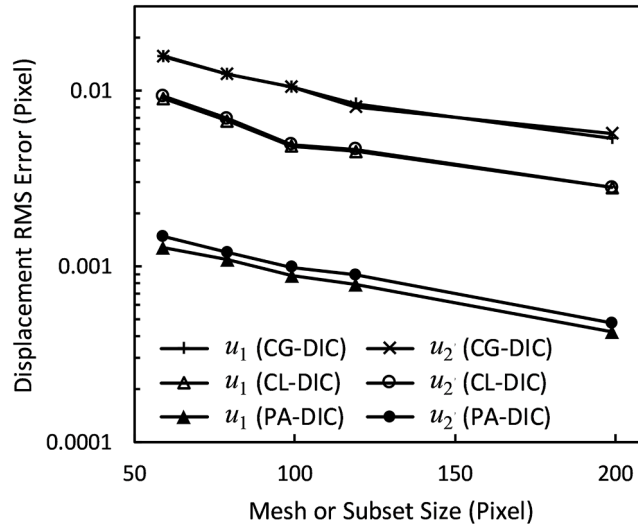
Fig. 7. Root-mean-square (RMS) errors in displacement measurement for CG-DIC, CL-DIC, and PA-DIC across different mesh/subset sizes.

errors is provided in Table 2. For the two conventional DIC methods, the displacement errors from the rigid-body rotation and stationary tests are very similar, suggesting that the measurement errors in both tests arise primarily from stochastic factors such as image acquisition noise and external vibrations. In contrast, for PA-DIC, the errors from the stationary test are approximately 30 % to 50 % of those from the rigid-body rotation test. This suggests that image acquisition noise and external vibrations account for a portion of the PA-DIC errors. The remaining errors stem from systematic factors related to the phase-shifting method, which is used to calculate the background and modulation intensities, as well as the initial speckle phase.

Fig. 7 illustrates the effects of subset/mesh size on displacement RMS errors for the three DIC methods. All the methods show a similar trend: as the subset/mesh size increases, the measurement accuracy improves with reduced RMS errors. This improvement results from the increased number of speckles for each correlation calculation, which helps to smooth out random pixel noise. We also note that CL-DIC and CG-DIC exhibit nearly identical RMS error levels in the horizontal and vertical directions. In contrast, the u_2 error curve of PA-DIC is somewhat higher than its u_1 error curve, which is attributed to the slightly lower measurement sensitivity in the vertical direction than in the horizontal direction ($|\Delta \mathbf{k}_2| < |\Delta \mathbf{k}_1|$). With comparable subset/mesh sizes, PA-DIC achieves displacement accuracy 5 to 7 times higher than CL-DIC and 9 to 12 times higher than CG-DIC, demonstrating its superior performance.

To further demonstrate the capability of PA-DIC, it was employed to assess non-uniform deformation in the TT specimen made of PMMA, which has an elastic modulus of 2.3 GPa and a Poisson's ratio of 0.36 (Dunn et al., 1997). Fig. 8(a) shows the non-uniform grid mesh structure used to discretize the ROI within the specimen, while Fig. 8(b) displays a photo of the specimen. The remaining subfigures display the measured displacement maps under a tensile load of 40 N, compared with those obtained by CL-DIC, CG-DIC, and FEM analyses. The PA-DIC measurement aligns closely with the FEM results. In comparison, the contour maps obtained with CL-DIC and CG-DIC capture the overall displacement pattern but exhibit considerable noise. We further evaluated the three DIC methods by comparing the strain fields from each method with the FEM results. Fig. 9(a1-a3) shows the contour plots of the three in-plane strain components from CL-DIC, obtained by numerically differentiating the displacement fields in Fig. 8(c1-c2) using the finite difference method. Although Gaussian filtering with a filter size of 50 pixels (0.69 mm) was applied to smooth these strain fields, they still exhibit significant noise and lack clear features due to the low signal-to-noise ratio (SNR) of the raw displacement fields. As shown in Fig. 9(b1-b3), increasing the filter size to 150 pixels (2.07 mm) helps to reduce the noise associated with the numerical differentiation, but the strain data still lack meaningful detail, particularly for the ε_{11} and ε_{22} components. The strain maps in Fig. 9 (c1-c3) and (d1-d3) were derived from the nodal displacements provided by CG-DIC and PA-DIC using the spatial derivatives of shape functions, without any smoothing or post-processing. The strain maps in Fig. 9(c1-c3) from CG-DIC exhibit high noise levels, similar to those from CL-DIC, which limit the clarity of the deformation features. In contrast, the tension-dominant deformation in the TT specimen is distinctly observed in the ε_{22} map from PA-DIC (Fig. 9(d2)), attributed to the high SNR provided by PA-DIC, even though the elastic deformation under measurement is extremely small (strain level $< 6 \times 10^{-4}$). Additionally, the strain maps in Fig. 9(d1-d3) accurately reveal the Poisson's ratio coupling between the ε_{11} and ε_{22} components, as well as the anti-symmetric shear strain (ε_{12}) distribution due to the tapering of the specimen. These observations align well with the computational strain fields from the FEM results in Fig. 9(e1-e3).

4.2. Learning constitutive law from PA-DIC measurement

In Fig. 10, we show the displacement and strain fields of the indentation specimen, acquired using PA-DIC at a peak compressive load of 40 N, which is sufficiently small to maintain elastic deformation. The build direction of the 3D-printed specimen is 45° with respect to the horizontal axis. Despite the symmetry in specimen geometry and loading conditions about the central vertical line, the
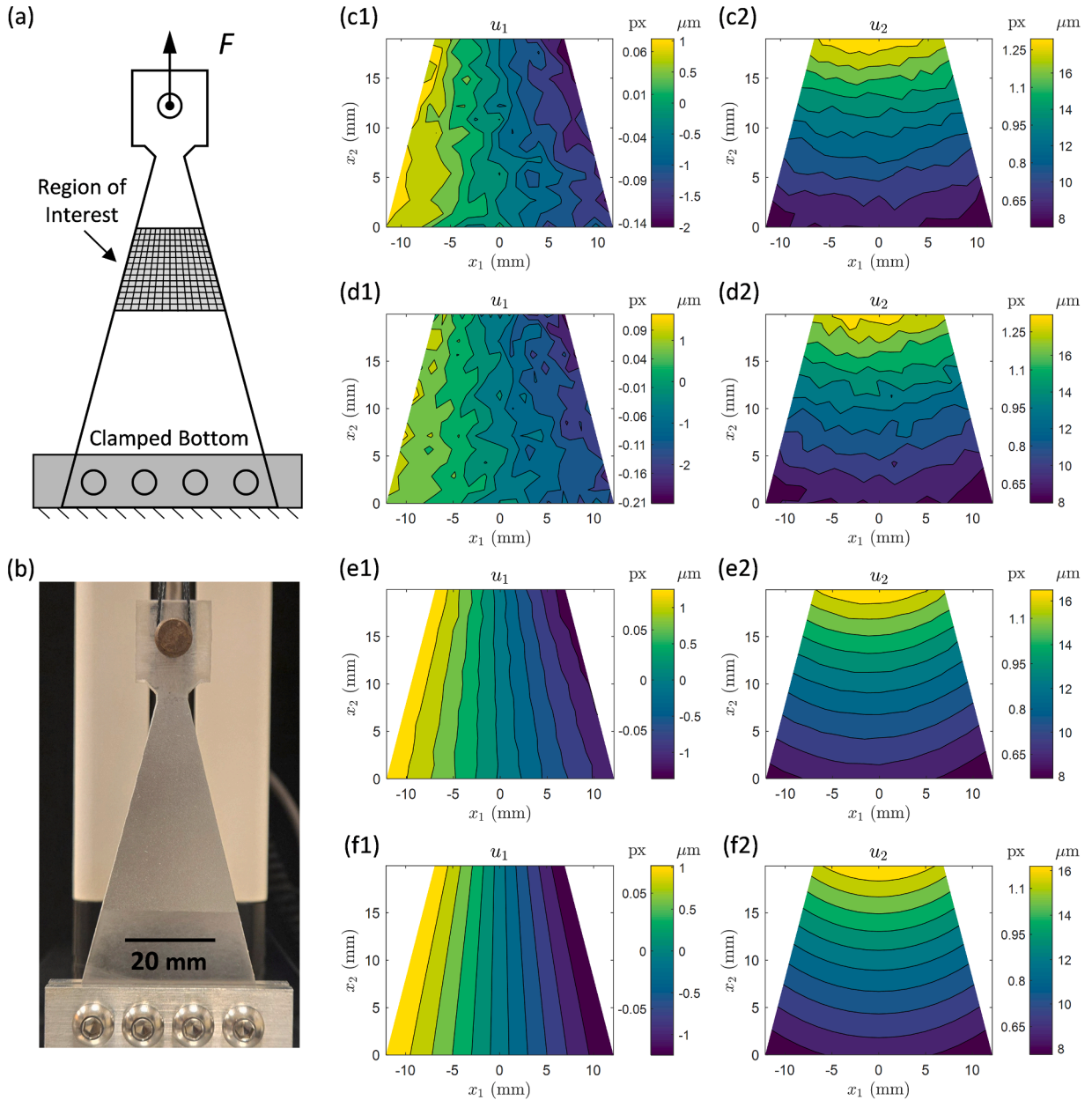
Fig. 8. (a) Tensile test of a tapered PMMA specimen with a uniform thickness of 3.1 mm. (b) Photo of the test specimen. Displacement contour plots for a tensile load of $F = 40$ N obtained from (c1-c2) CL-DIC, (d1-d2) CG-DIC, (e1-e2) PA-DIC, and (f1-f2) FEM analysis.

contour maps in Fig. 10, especially those for u_2, ε_{11}, and ε_{22}, are noticeably non-symmetric, qualitatively indicating elastic anisotropy. The experimental strain data within the ROI from 10 uniform loading steps ($F = 4$ to 40 N) were used in the loss function (Eq. (11)) to train three MINN models with an increasing number of neurons in the hidden layer: $5 \times 3 \times 1$, $5 \times 12 \times 1$, and $5 \times 48 \times 1$. The training loss of the three models is shown in Fig. 11. The results show that the performance of the MINN models exhibits excellent stability as the model complexity varies. Additionally, models with larger sizes have similar convergence rates and do not significantly reduce the loss.

To validate the performance of the trained constitutive models, the orthotropic angle (φ) and the elastic constants, including elastic moduli in the build and layer directions (E_1 and E_2), shear moduli (G_{12}), and Poisson's ratio (ν_{12}), were derived from the trained strain energy density (W) and are listed in Table 3. Also shown in the table for comparison are the elastic properties measured separately as the ground truth using uniaxial tensile tests on dog-bone specimens, following the testing protocol outlined in Zhao et al. (2019). Our MINN models provide accurate predictions for the orthotropic direction of the material, as well as the anisotropy ratio (E_2/E_1), G_{12}, and ν_{12}, with relative errors <2.5 %. The relative errors in predicting the values of E_1 and E_2 are higher, ranging from 10 % to 14 %.
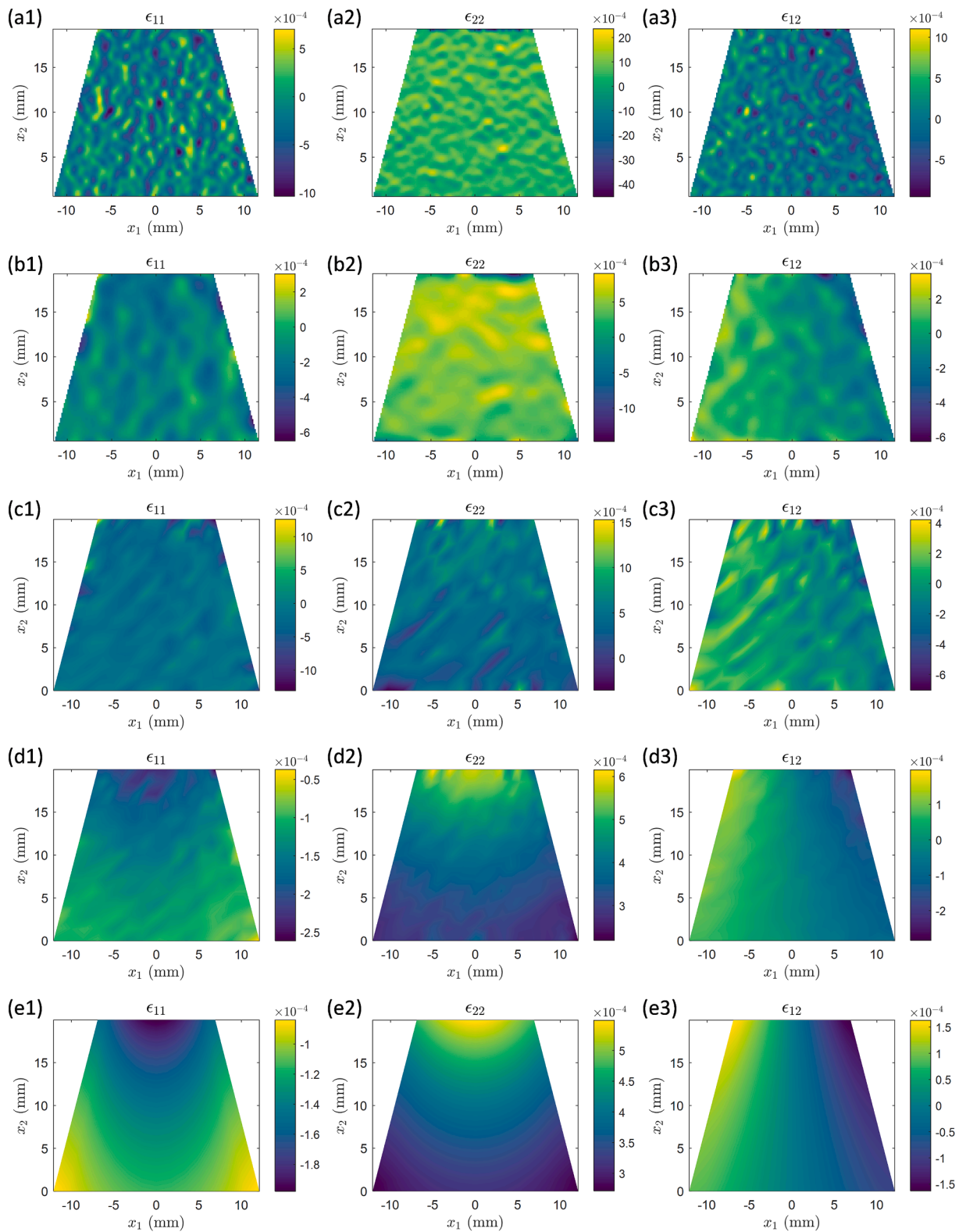
Fig. 9. Strain maps of the tapered specimen obtained from (a1-a3) CL-DIC with a Gaussian filter size of 50 pixels (0.69 mm), (b1-b3) CL-DIC with a Gaussian filter size of 150 pixels (2.07 mm), (c1-c3) CG-DIC, (d1-d3) PA-DIC, and (e1-e3) FEM analysis.
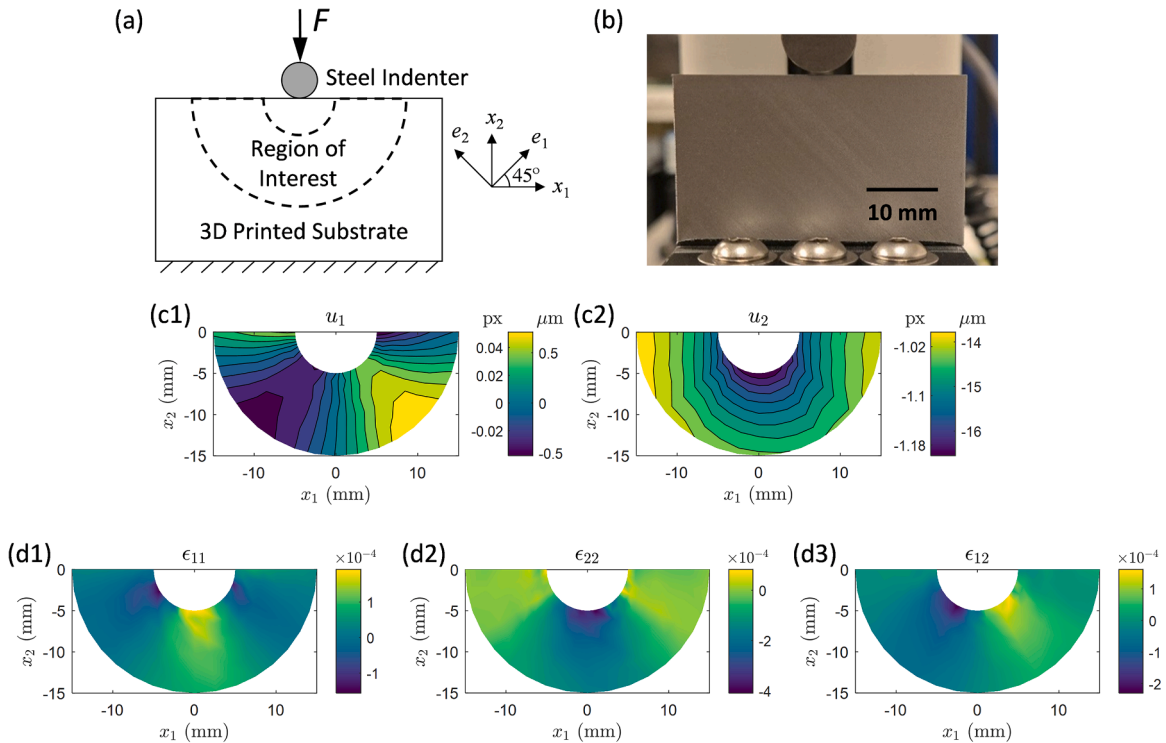
Fig. 10. (a) Indentation test of a 3D printed carbon fiber-reinforced PLA substrate with a uniform thickness of 3.9 mm. The lower-right corner shows the global coordinate system (x_1-x_2) and the material coordinate system (e_1-e_2), with e_1 as the build direction and e_2 as the layer direction. (b) Photo of the test specimen. (c1-c2) Displacement contour plots for an indentation load of $F = 40$ N measured by PA-DIC. (d1-d3) Strain maps calculated from the measured displacement components.
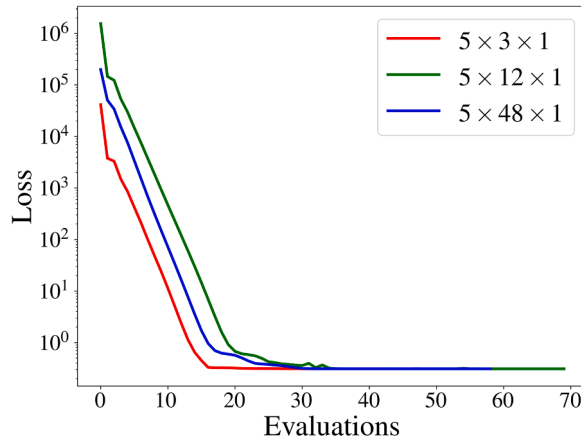

Fig. 11. Training loss for three MINN architectures with increasing model complexity. The maximum number of iterations was set to 100. During each iteration, the loss was evaluated multiple times until it was smaller than in the previous step.

One significant source of such increased errors is the sample-to-sample variation. The indentation and dog-bone specimens were fabricated via 3D printing in different batches. Although nominally consistent printing conditions were specified, the software used for slicing 3D prints made automatic adjustments to the printing speed to refine the geometrical accuracy of each printed layer. This may affect the printed microstructure and, as a result, the corresponding mechanical properties. Other possible reasons include: (i) discrepancies between the real experimental setup and the boundary conditions used in FEM modeling; and (ii) the finite thickness of the indentation specimen, which, although intentionally smaller than the characteristic in-plane dimensions, can still result in the overestimation of E_1 and E_2 due to the plane-stress assumption.

The displacement and strain contour plots from the MINN model ($5 \times 3 \times 1$), after training on the experimental PA-DIC data, are

Table 3

Comparison between the experimentally measured material parameters of 3D printed PLA and the values predicted by the MINN models. Here, Poisson's ratio ν_{ij} represents the ratio of strain in the *j*-direction to strain in the *i*-direction under uniaxial stress along *i*.

	E_1(**MPa**)	E_2(**MPa**)	E_2/E_1	G_{12}(**MPa**)	ν_{12}	φ(∘)
Experiments	2860	4540	1.59	1050	0.25	45.0
MINN (5 × 3 × 1)	3157	5161	1.63	1073	0.27	45.3
MINN (5 × 12 × 1)	3157	5161	1.63	1073	0.27	45.3
MINN (5 × 48 × 1)	3157	5161	1.63	1073	0.27	45.3

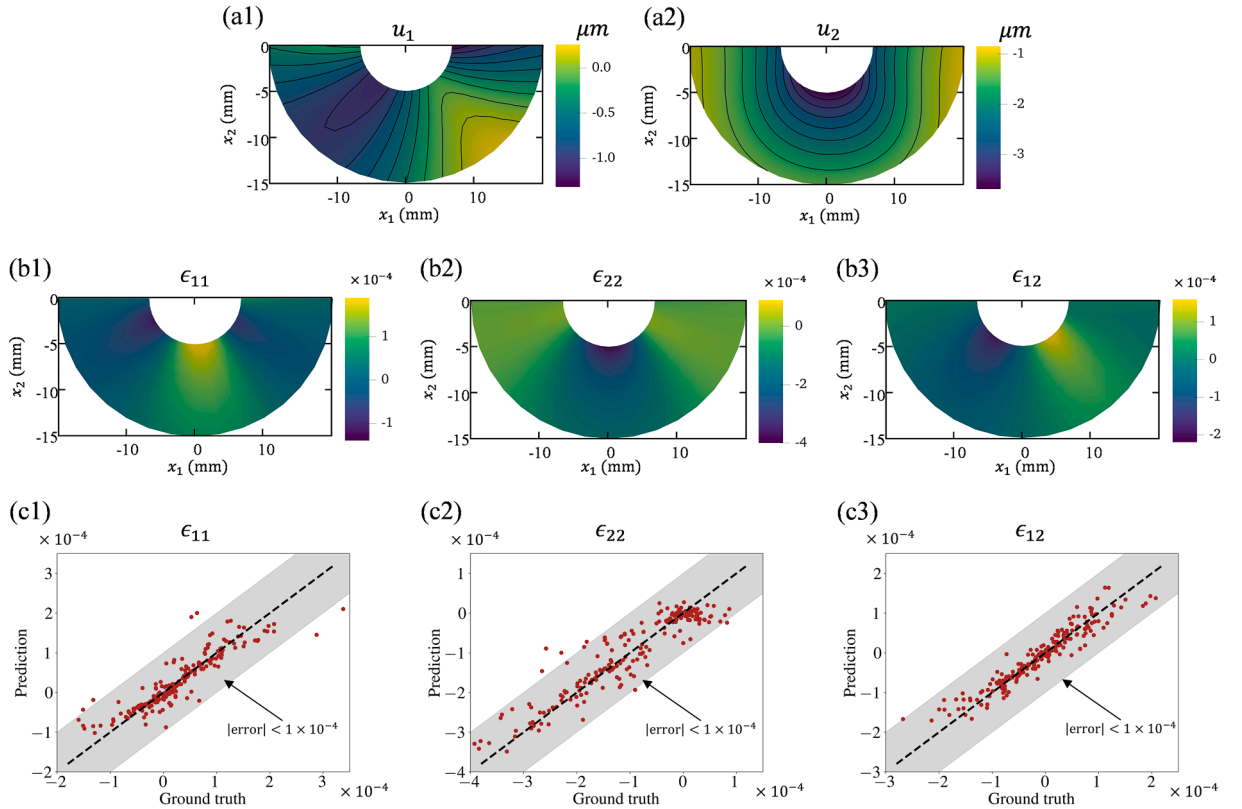**Fig. 12.** (a1-a3) Displacement and (b1-b3) strain contour plots obtained from MINN (5 × 3 × 1) predictions for an indentation load of $F = 40$ N. (c1-c3) Comparisons of strain measurements from PA-DIC with strain predictions from MINN (5 × 3 × 1).

shown in Fig. 12(a1-b3). Comparing the trained displacement contour plots with the experimental ones in Fig. 10(c1-c2) reveals a rigid-body motion (~ 0.5 μm horizontally and ~ 13 μm vertically), attributed to the movement of the specimen support during the experiment. Since this rigid-body motion does not affect strain calculations, the three MINN models trained with the strain data accurately identify the material parameters and reproduce the strain response with a maximum prediction error of approximately 1×10^{-4} in the entire ROI, as shown in Fig. 12(c1-c3).

5. Discussion

PA-DIC provides a novel means for deformation measurement by combining the full-field measurement capability of DIC with the high sensitivity of optical interferometry. Our validation tests have demonstrated that PA-DIC significantly reduces measurement errors compared to conventional DIC. While conventional DIC is inherently length scale independent, the measurement sensitivity of PA-DIC scales with the magnitude of the wave-vector difference $|\Delta\mathbf{k}|$. This scaling behavior suggests that adjusting the light wavelength and illumination angles can further enhance the performance of PA-DIC. Such enhancement would come with increased stability requirements, necessitating greater care to minimize ambient vibrations and imaging noise. The current PA-DIC setup is limited to 2D in-plane displacement measurement. By introducing additional illuminating beams with a wave-vector difference that includes an out-of-plane component, phase sensitivity to out-of-plane displacements can be achieved to enable 3D full-field displacement

measurement. We acknowledge that the implementation of PA-DIC requires coherent illumination, adding to the complexity and alignment requirements of optical setups. These issues can be mitigated by employing low-cost diode laser sources and fiber optic components for beam splitting and routing, which greatly simplifies the measurement procedure and reduces costs. Furthermore, the background and modulation intensities in the undeformed state (Eq. (1)) needed for image correlation can be obtained using arbitrary phase-shifting techniques (Kemao et al., 2010; Wang and Han, 2004). This would eliminate the need for costly nano-positioning systems for fixed-step phase shifting.

A notable feature of PA-DIC is that it does not require spatial phase shifting during image acquisition at each deformation stage, unlike traditional interferometric measurement techniques that typically rely on phase shifting and are thus limited to quasi-static measurement. Instead, PA-DIC obtains displacements from phase information by directly correlating images taken before and after deformation, in a manner similar to conventional DIC. Consequently, when combined with high-speed photography, PA-DIC can be readily applied for dynamic full-field measurement, although the measurement rate is halved due to alternating measurements along the x_1- and x_2-directions. It is also worth noting that the phase retrieval scheme we employed is based on the minimization of the cost function with respect to both the sine and cosine of the displacement components, as well as the displacement components themselves (see Eq. (5)). This approach helps maintain the convexity of the cost function to ensure efficient minimization. The minimization yields not only high-accuracy speckle phases wrapped modulo 2π, but also raw displacements with lower sensitivity as offered by conventional DIC. This low-sensitivity displacement information is currently discarded but can be harnessed for rapid phase unwrapping to remove phase ambiguities. We will explore this in future work.

The hybrid FEM-NN optimization framework presented in this work represents an efficient use of the high-accuracy, non-uniform deformation data provided by PA-DIC. Compared with conventional testing approaches for anisotropic materials, which require multiple tests under different loading conditions, the hybrid FEM-NN method is advantageous for efficiently identifying material parameters from a single set of experimental data. Specifically, even when the anisotropy orientation is unknown a priori, our method can still provide accurate predictions based on the high-accuracy inhomogeneous deformation data from PA-DIC.

6. Conclusion

We have developed PA-DIC as a new method for full-field deformation measurement. By utilizing coherent illumination and image correlation for phase retrieval, the proposed method is able to achieve ultra-high measurement accuracy that significantly surpasses that of conventional DIC. The validity and accuracy of the method have been verified through testing of rigid-body rotation and non-uniform tensile deformation. Additionally, its utility has been demonstrated through the hybrid FEM-NN learning of an orthotropic elastic constitutive law from the inhomogeneous strain fields measured by PA-DIC. With its exceptional measurement accuracy, PA-DIC opens new possibilities for high-precision mechanical testing and data-driven characterization of materials and structures in the small deformation regime.

CRediT authorship contribution statement

Rahul Danda: Writing – review & editing, Writing – original draft, Visualization, Validation, Methodology, Investigation, Formal analysis, Conceptualization. **Xinxin Wu:** Writing – review & editing, Writing – original draft, Validation, Methodology, Investigation, Formal analysis. **Sheng Mao:** Writing – review & editing, Writing – original draft, Supervision, Methodology, Investigation, Formal analysis. **Yin Zhang:** Writing – review & editing, Writing – original draft, Supervision, Methodology, Investigation, Formal analysis. **Ting Zhu:** Writing – review & editing, Methodology, Investigation, Formal analysis. **Shuman Xia:** Writing – review & editing, Writing – original draft, Supervision, Project administration, Methodology, Investigation, Formal analysis, Data curation, Conceptualization.

Declaration of competing interest

The authors declare that they have no known competing financial interests or personal relationships that could have appeared to influence the work reported in this paper.

Appendix: Convergence analysis of the phase retrieval algorithm

We consider a one-dimensional (1D) model specimen to analyze the convergence of displacement calculation for the phase retrieval algorithm detailed in Section 2.1. The specimen has a speckle phase distribution of $\gamma(X) = \frac{2\pi X}{s}$, where s is the speckle size and X is the coordinate. Assuming unit background and modulation intensities, the speckle intensity in the initial configuration is a periodic function given by

$$f(X) = 1 + \cos(\gamma(X)) = 1 + \cos\left(\frac{2\pi X}{s}\right). \tag{A1}$$

The specimen is then subjected to a rigid-body translation of u_0, and the speckle intensity, accounting for both the speckle movement and the change in speckle phase, becomes

$$g(X) = 1 + \cos\left[\frac{2\pi(X - u_0)}{s} + \Delta k u_0\right]. \tag{A2}$$

For the above 1-D system, the squared residual error (Eq. (3)) and residual (Eq. (4)) reduce to

$$E^2 = \int_0^s \left\{1 + \cos\left(\frac{2\pi X}{s} + \Delta k u\right) - g(X + u)\right\}^2 dX, \tag{A3}$$

and

$$E \approx \cos\left(\frac{2\pi X}{s} + \Delta k u^{(n)}\right)\cos(\Delta k \delta u) - \sin\left(\frac{2\pi X}{s} + \Delta k u^{(n)}\right)\sin(\Delta k \delta u)$$

$$- \cos\left(\frac{2\pi(X + u^{(n)} - u_0)}{s} + \Delta k u_0\right) + \frac{l}{s}\sin\left(\frac{2\pi(X + u^{(n)} - u_0)}{s} + \Delta k u_0\right)(\Delta k \delta u), \tag{A4}$$

where $l = \frac{2\pi}{\Delta k}$ is a characteristic length determined by the wave-vector difference Δk. Using the phase retrieval scheme presented in Section 2.1, the displacement can be obtained by minimizing Eq. (A3) with respect to $p = \cos(\Delta k \delta u)$, $q = \sin(\Delta k \delta u)$, and $\Delta k \delta u$.

From Eq. (A4), we observe that $\frac{l}{s}$ dictates the sensitivity ratio of the residual with respective to (p, q) and $\Delta k \delta u$. When $\frac{l}{s} << 1$ (i.e., the speckle size is sufficient large), the residual becomes significantly more sensitive to the phase change than to the speckle movement. Therefore, although to (p, q) and $\Delta k \delta u$ are theoretically dependent, they effectively act as pseudo-independent variables in the minimization of Eq. (A3). Fig. A1(a) shows the displacement error as a function of the number of iterations for a prescribed $u_0 = \frac{\pi}{2\Delta k}$. It is evident that when $\frac{l}{s} \leq 0.1$, fast convergence is guaranteed. Meanwhile, the constraint $p^2 + q^2 = \cos^2(\Delta k \delta u) + \sin^2(\Delta k \delta u) = 1$ is automatically satisfied through the minimization of Eq. (A3), as demonstrated in Fig. A1(b).
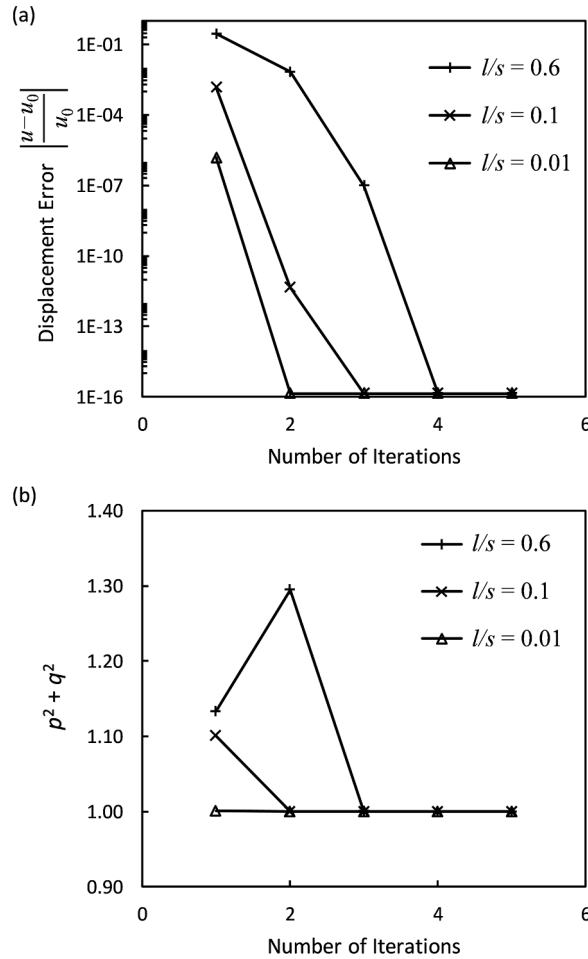

Fig. A1. Convergence analysis of the phase retrieval algorithm. (a) Displacement error as a function of the number of iterations, and (b) validation of the constraint $p^2 + q^2 = 1$ achieved through the iterative minimization of the squared residual error (Eq. (A3)).

Data availability

Data will be made available on request.

References

Alnæs, M., Blechta, J., Hake, J., Johansson, A., Kehlet, B., Logg, A., Richardson, C., Ring, J., Rognes, M.E., Wells, G.N., 2015. The FEniCS project version 1.5. Archive of numerical software 3.

Amos, B., Xu, L., Kolter, J.Z., 2017. Input convex neural networks. In: International conference on machine learning. PMLR, pp. 146–155.

Avril, S., Bonnet, M., Bretelle, A.-S., Grediac, M., Hild, F., Ienny, P., Latourte, F., Lemosse, D., Pagano, S., Pagnacco, E., 2008. Overview of identification methods of mechanical parameters based on full-field measurements. Exp. Mech. 48, 381–402.

Besnard, G., Hild, F., Roux, S., 2006. Finite-element" displacement fields analysis from digital images: application to Portevin–Le Châtelier bands. Exp. Mech. 46, 789–803.

Boddapati, J., Flaschel, M., Kumar, S., De Lorenzis, L., Daraio, C., 2023. Single-test evaluation of directional elastic properties of anisotropic structured materials. J. Mech. Phys. Solids 181, 105471.

Byrd, R.H., Lu, P., Nocedal, J., Zhu, C., 1995. A limited memory algorithm for bound constrained optimization. SIAM J. Sci. Comput. 16, 1190–1208.

Chasiotis, I., Knauss, W.G., 2002. A new microtensile tester for the study of MEMS materials with the aid of atomic force microscopy. Exp. Mech. 42, 51–57.

Chu, T., Ranson, W., Sutton, M., 1985. Applications of digital-image-correlation techniques to experimental mechanics. Exp. Mech. 25, 232–244.

Cloud, G.L., 1998. Optical Methods of Engineering Analysis. Cambridge University Press.

Delacourt, C., Allemand, P., Casson, B., Vadon, H., 2004. Velocity field of the "La Clapière" landslide measured by the correlation of aerial and QuickBird satellite images. Geophys. Res. Lett. 31.

Dunn, M.L., Suwito, W., Cunningham, S., 1997. Fracture initiation at sharp notches: correlation using critical stress intensities. Int. J. Solids Struct. 34, 3873–3883.

Ferreira, R.T.L., Amatte, I.C., Dutra, T.A., Bürger, D., 2017. Experimental characterization and micrography of 3D printed PLA and PLA reinforced with short carbon fibers. Compos. Part B: Eng. 124, 88–100.

Flaschel, M., Kumar, S., De Lorenzis, L., 2022. Discovering plasticity models without stress data. npj Comput. Mater. (Basel) 8, 91.

Ghiglia, D.C., Romero, L.A., 1994. Robust two-dimensional weighted and unweighted phase unwrapping that uses fast transforms and iterative methods. JOSA A 11, 107–117.

Grediac, M., 2004. The use of full-field measurement methods in composite material characterization: interest and limitations. Compos., Part A 35, 751–761.

Hild, F., Roux, S., 2012. Comparison of local and global approaches to digital image correlation. Exp. Mech. 52, 1503–1519.

Hughes, T.J., 2003. The Finite Element Method: Linear Static and Dynamic Finite Element Analysis. Courier Corporation.

Hung, Y., Ho, H., 2005. Shearography: an optical measurement technique and applications. Mater. Sci. Eng.: R: Reports 49, 61–87.

Johnson, C., Ruud, J., Bruce, R., Wortman, D., 1998. Relationships between residual stress, microstructure and mechanical properties of electron beam–physical vapor deposition thermal barrier coatings. Surf. Coat. Technol. 108, 80–85.

Kammers, A.D., Daly, S., 2013. Digital image correlation under scanning electron microscopy: methodology and validation. Exp. Mech. 53, 1743–1761.

Kemao, Q., Wang, H., Gao, W., Feng, L., Soon, S.H., 2010. Phase extraction from arbitrary phase-shifted fringe patterns with noise suppression. Opt. Lasers Eng. 48, 684–689.

Klein, D.K., Fernández, M., Martin, R.J., Neff, P., Weeger, O., 2022. Polyconvex anisotropic hyperelasticity with neural networks. J. Mech. Phys. Solids 159, 104703.

Krehbiel, J.D., Lambros, J., Viator, J., Sottos, N., 2010. Digital image correlation for improved detection of basal cell carcinoma. Exp. Mech. 50, 813–824.

Linden, L., Klein, D.K., Kalina, K.A., Brummund, J., Weeger, O., Kästner, M., 2023. Neural networks meet hyperelasticity: a guide to enforcing physics. J. Mech. Phys. Solids 179, 105363.

McClung, A.J., Tandon, G., Goecke, K., Baur, J., 2011. Non-contact technique for characterizing full-field surface deformation of shape memory polymers at elevated and room temperatures. Polym. Test. 30, 140–149.

Mitusch, S., Funke, S., Dokken, J., 2019. dolfin-adjoint 2018.1: automated adjoints for FEniCS and Firedrake. J. Open Source Software 4, 1292.

Nave, M.D., Barnett, M.R., 2004. Microstructures and textures of pure magnesium deformed in plane-strain compression. Scr. Mater. 51, 881–885.

Pan, B., Qian, K., Xie, H., Asundi, A., 2009. Two-dimensional digital image correlation for in-plane displacement and strain measurement: a review. Meas. Sci. Technol. 20, 062001.

Pan, B., Wang, B., Lubineau, G., Moussawi, A., 2015. Comparison of subset-based local and finite element-based global digital image correlation. Exp. Mech. 55, 887–901.

Peters, W., Ranson, W., 1982a. Digital imaging techniques in experimental stress analysis. Opt. Eng. 21, 427–431.

Peters, W.H., Ranson, W.F., 1982b. Digital imaging techniques in experimental stress-analysis. Opt. Eng. 21, 427–431.

Rastogi, P., 2000. Photomechanics. Springer, Berlin.

Sun, Y., Pang, J.H., Wong, C.K., Su, F., 2005. Finite element formulation for a digital image correlation method. Appl. Opt. 44, 7357–7363.

Sutton, M., Wolters, W., Peters, W., Ranson, W., McNeill, S., 1983. Determination of displacements using an improved digital correlation method. Image Vision Comput. 1, 133–139.

Sutton, M.A., Cheng, M.Q., Peters, W.H., Chao, Y.J., Mcneill, S.R., 1986. Application of an optimized digital correlation method to planar deformation analysis. Image Vision Comput. 4, 143–150.

Tac, V., Costabal, F.S., Tepole, A.B., 2022. Data-driven tissue mechanics with polyconvex neural ordinary differential equations. Comput. Methods Appl. Mech. Eng. 398, 115248.

Thakolkaran, P., Joshi, A., Zheng, Y., Flaschel, M., De Lorenzis, L., Kumar, S., 2022. NN-EUCLID: deep-learning hyperelasticity without stress data. J. Mech. Phys. Solids 169, 105076.

Tung, C.-H., Li, J., 2024. The anti-dogbone: evaluating and designing optimal tensile specimens for deep learning of constitutive relations. Extreme. Mech. Lett. 69, 102157.

Wang, X., Pan, Z., Fan, F., Wang, J., Liu, Y., Mao, S.X., Zhu, T., Xia, S., 2015. Nanoscale deformation analysis with high-resolution transmission electron microscopy and digital image correlation. J. Appl. Mech. 82, 121001.

Wang, Z., Han, B., 2004. Advanced iterative algorithm for phase extraction of randomly phase-shifted interferograms. Opt. Lett. 29, 1671–1673.

Wu, X., Sun, K., Yang, S., Wang, H., Xu, Y., Zhang, Y., Mao, S., 2024. A hybrid FEM-NN optimization method to learn the physics-constrained constitutive relations from full-field data. arXiv e-prints, arXiv: 2406.16457.

Yang, J., Bhattacharya, K., 2019a. Augmented lagrangian digital image correlation. Exp. Mech. 59, 187–205.

Yang, J., Bhattacharya, K., 2019b. Fast adaptive global digital image correlation. In: Advancement of Optical Methods & Digital Image Correlation in Experimental Mechanics, 3. Springer, pp. 69–73.

Zhang, Y., Li, Q.-J., Zhu, T., Li, J., 2022. Learning constitutive relations of plasticity using neural networks and full-field data. Extreme Mech. Lett. 52, 101645.

Zhao, Y., Chen, Y., Zhou, Y., 2019. Novel mechanical models of tensile strength and elastic property of FDM AM PLA materials: experimental and theoretical analyses. Mater. Des. 181, 108089.